

# **Growth and Investigation of Ferromagnetic and Antiferromagnetic Quantum Materials for Spintronic Devices**

**Kacho Imtiyaz Ali Khan**



DEPARTMENT OF PHYSICS,  
INDIAN INSTITUTE OF TECHNOLOGY DELHI  
JULY 2023

© Indian Institute of Technology Delhi (IITD), New Delhi, 2023

# Growth and Investigation of Ferromagnetic and Antiferromagnetic Quantum Materials for Spintronic Devices

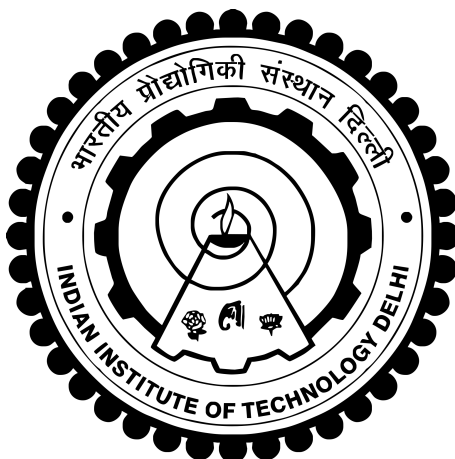
by

**Kacho Imtiyaz Ali Khan**

Department of Physics

Submitted

in fulfilment of the requirements for the degree of the Doctor of Philosophy  
to the



INDIAN INSTITUTE OF TECHNOLOGY DELHI

JULY 2023

## Certificate

This is to certify that the thesis entitled, **Growth and Investigation of Ferromagnetic and Antiferromagnetic Quantum Materials for Spintronic Devices**, being submitted by **Mr. Kacho Imtiyaz Ali Khan** to the Department of Physics, Indian Institute of Technology Delhi, for the award of the degree of **Doctor of Philosophy** is a record of bonafide work carried out by him. He has worked under our supervision and guidance and has fulfilled the requirements for the submission of this thesis, which in our opinion has reached the requisite standard.

The results contained in this thesis have not been submitted, in part or full, to any other University or Institute for the award of any degree/diploma.

---

**Prof. Pranaba Kishor Muduli**

Professor

Department of Physics

Indian Institute of Technology Delhi

New Delhi - 110016, India.

Date:

## Acknowledgements

I would like to express my gratitude to everyone who made my Ph.D. journey smoother through their deliberate support, guidance, and encouragement to complete this unforgettable journey. First and foremost, I would like to express my sincere gratitude towards my supervisor Prof. P. K. Muduli for providing the needed guidance, inspiration, and moral & financial support needed to carry out the research work. I sincerely thank the Student Research Committee (SRC) members: Prof. Neeraj Khare, Prof. Pintu Das, and Prof. Debanjan Bhowmik for their scientific advice and comments while adding their valuable suggestions and input during my SRC presentations.

I am particularly thankful to Prof. Prasanta Kumar Muduli (IIT Madras) for helping me with the fruitful scientific discussions regarding various transport measurements. I am privileged to have the opportunity to begin my Ph.D. journey under the guidance of my seniors, Dr. Raghav Sharma, Dr. Naveen Sisodia, Dr. Akash Kumar, and Dr. Niru Chowdhury. I also want to thank my present labmates: Pankhuri, Ram, Himanshu, Rekha, Richa, Neha, and Nidhi for making a memorable and maintaining a friendly environment in the lab. Special thanks to my senior Dr. Naveen Sisodia, who guided me well in acquainting me with the basics of micromagnetic simulation including coding in Mumax3 and MATLAB scripts for numerical analyses. I am extremely thankful to my senior Dr. Akash Kumar, who assisted me with the experimental setup and for fruitful scientific discussions and suggestions throughout my Ph.D. progress work. I also acknowledge Dr. Niru Chowdhury for the proofreading part that she did in this thesis and other published research articles. I thank my IIT Delhi batch mates and other friends; Abid, Dechen, Tsering, Prashant, Aditya, Mansi, Nida, Gazal, Upasana, Balram, Deeksha, and Soumyaroop for the wonderful memory we shared during the Ph.D. journey. A special thanks to my childhood friend Shabir for always providing me encouragement on trying days. I also thank my friend Deeksha Khandelwal for being a constant inspiration for me to look at remarkable opportunities. A final note of thanks to all the members of Thin Film Laboratory, IIT-Delhi for organizing various scientific events during this Ph.D. journey.

I am thankful to Nanoscale Research Facility (NRF) and Central Research Facility (CRF) at IIT Delhi for providing me with various essential instruments for the characterization of samples and providing software resources for helping me to execute my research work smoothly. I also thank IIT Delhi for giving me access to software resources (such as OriginPro, Team-viewer, MATLAB, Overleaf, and MS Office) and High-Performance Computing (HPC) facilities for computational resources. I thank IIT Delhi for providing me research scholar travel award

(RSTA) grant to present my research works at an international conference, Magnetism and Magnetic Materials (MMM), Las Vegas, United States of America (USA), and the research excellence travel award (RETA) grant for the conference SolskyMag2022, Spain. I acknowledge the University Grant Commission (UGC) for financial support during my Ph.D. I also want to thank the Department of Science and Technology (DST), Science and Engineering Research Board (SERB), Government of India for providing the travel grant to present my research work at an international conference JEMS2022, Warsaw, Poland.

At last, I would like to express my gratitude and appreciation to my family members; my brother Dr. Kacho Amir Khan for his continuous guidance and inspiration in achieving my goals in this journey; my sisters Chocho Fatima Khanam, Chocho Najma, and Chocho Zainab Huriya for their continuous care and appreciation along this path. A special to my parents Kacho Ahmad Khan and Chocho Kulsum for raising me with their boundless love, support, and blessings, they were the major source of inspiration throughout my life. I am thankful to the almighty for the countless blessings bestowed upon me and for giving me the mental and physical strength to accomplish the Ph.D. journey.

*I want to dedicate this thesis to my lovely parents*

*Kacho Imtiyaz Ali Khan*

# Abstract

Topological quantum materials are extremely promising for next-generation of spintronic devices such as magnetic memories due to their non-trivial band topology. Recently, kagome ferromagnet (FM)  $\text{Fe}_3\text{Sn}_2$  and antiferromagnet (AFM)  $\text{FeSn}$ , which belong to the  $\text{Fe}_n\text{Sn}_m$ -family ( $m : n = 1:1, 3:2, 5:3$ ) have emerged as the promising magnetic quantum materials due to their intriguing topological properties, such as the presence of Dirac nodes, Weyl points, flat bands, and topological surface states in their band structure. To date, most of the experimental and theoretical studies on  $\text{Fe}_3\text{Sn}_2$  and  $\text{FeSn}$  have been predominantly concentrated on bulk single crystals. However, the experimental realization of the thin film of these materials with stable phase and stoichiometry is challenging. Thin films of these materials and their heterostructures are desirable for spintronics-based device applications. The topological and quantum properties can be further tuned in thin films through reduced dimensionality. In addition, thin films allow the creation of heterostructures with other materials, which may host emergent phenomena. This motivated us to investigate the growth of thin films of  $\text{Fe}_3\text{Sn}_2$  and  $\text{FeSn}$  and their heterostructures for spintronics applications. In this thesis, we establish the growth of thin films of ferromagnetic  $\text{Fe}_3\text{Sn}_2$  and antiferromagnetic  $\text{FeSn}$  and  $\text{NiO}$  thin films. Subsequently, we grow heterostructures of these materials with either heavy metal or ferromagnet (in the case of  $\text{FeSn}$  and  $\text{NiO}$ ) to study spin pumping behavior, which is technologically important for next-generation magnetic recording devices.

In the case of  $\text{Fe}_3\text{Sn}_2$ , we first demonstrate the growth of polycrystalline ferromagnetic  $\text{Fe}_3\text{Sn}_2$  thin films on  $\text{Si}/\text{SiO}_2$  substrates by using a Pt seed layer. Our structural and magnetic measurements indicate that a pure ferromagnetic phase of  $\text{Fe}_3\text{Sn}_2$  thin films with higher saturation magnetization of  $M_S = 464 - 640$  emu/cc is formed for the Pt seed layer, while a mixed-phase (consisting of ferromagnetic  $\text{Fe}_3\text{Sn}_2$  and antiferromagnetic  $\text{FeSn}$ ) with a lower  $M_S$  is formed for the Ta seed layer. The anomalous Hall effect measurements were performed to determine the role of the electronic bands due to the kagome structure of  $\text{Fe}_3\text{Sn}_2$ . We found a non-zero intrinsic anomalous Hall conductivity ( $\sigma_{xy}^{int}$ ), a large value anomalous Hall coefficient ( $R_S$ ), and anomalous Hall angle ( $\theta_{AHA}$ ) indicating the intrinsic origin of anomalous Hall resistivity in  $\text{Fe}_3\text{Sn}_2$  thin films. The ferromagnetic resonance study performed in Pt/ $\text{Fe}_3\text{Sn}_2$  based heterostructure allows us to determine intrinsic damping of  $\text{Fe}_3\text{Sn}_2$  to be  $\alpha_{int.} = (3.8 \pm 0.2) \times 10^{-2}$ . Furthermore, the spin mixing conductance of Pt/ $\text{Fe}_3\text{Sn}_2$  is found to be  $g_{eff}^{\uparrow\downarrow} = (11.7 \pm 0.6) \text{ nm}^{-2}$ , which is comparable to other ferromagnet/heavy metal systems.

In the case of  $\text{FeSn}$ , we demonstrate epitaxial growth using the Pt seed layer on the sapphire

substrate. The antiferromagnetic phase was confirmed using magnetization measurements as well as the presence of exchange bias in FeSn/Ni<sub>80</sub>Fe<sub>20</sub> bilayers. A large spin mixing conductance of  $g_{\text{eff}}^{\uparrow\downarrow} = (117 \pm 0.6) \text{ nm}^{-2}$  is found in FeSn/Py which is nearly two-order of magnitude higher compared to the standard ferromagnet/heavy metal systems. The large value of  $g_{\text{eff}}^{\uparrow\downarrow}$  is promising for application and indicates the possible role of the kagome lattice of FeSn. We have also investigated the spin pumping in the antiferromagnet NiO/Py system and we showed that the  $g_{\text{eff}}^{\uparrow\downarrow}$  of an optimized polycrystalline-NiO/Py system can reach the value that for an epitaxial-NiO/Py system.

In the final part of the thesis, we numerically explore the potential application of magnetic quantum material-based heterostructures. Magnetic skyrmions are highly promising for the next generation of racetrack memory devices as they offer ultra-dense storage capacity and low power consumption in comparison to domain-wall based racetrack memory devices. In this thesis, we numerically studied the nucleation process of the FM and AFM skyrmions in racetrack devices. We found an ultrafast nucleation single/multiple AFM skyrmion using in-plane spin-polarized current in an AFM material. In addition, our method also shows low energy consumption for nucleation using in-plane spin-polarized current compared to out-of-plane spin-polarized current. We stabilize FM skyrmion for a range of external magnetic fields in ferromagnet Fe<sub>3</sub>Sn<sub>2</sub> without using Dzyaloshinskii–Moriya interaction. The strong uniaxial magnetic anisotropy and dipole-dipole interaction of the kagome lattice in Fe<sub>3</sub>Sn<sub>2</sub> facilitate the nucleation of both skyrmions and anti-skyrmions.

## सारांश

टोपोलॉजिकल क्वांटम पदार्थ अपने गैर-तुच्छ बैंड टोपोलॉजी के कारण अगली पीढ़ी के स्पिट्रॉनिक उपकरणों जैसे चुंबकीय यादों के लिए बेहद आशाजनक हैं। हाल ही में, कागोम लौहचुंबकीय (FM)  $\text{Fe}_3\text{Sn}_2$  और प्रतिलौहचुंबकीय (AFM)  $\text{FeSn}$ , जो  $\text{Fe}_m\text{Sn}_n$ -परिवार ( $m : n :: 1:1, 3:2, 5:3$ ) से संबंधित हैं, अपने पेचीदा टोपोलॉजिकल गुणों जैसे कि डिराक नोड्स, वेइल पॉइंट, फ्लैट बैंड और टोपोलॉजिकल सतह स्थितियों की उपस्थिति के कारण आशाजनक चुंबकीय क्वांटम पदार्थ के रूप में उभरे हैं। आज तक  $\text{Fe}_3\text{Sn}_2$  और  $\text{FeSn}$  पर अधिकांश प्रयोगात्मक और सैद्धांतिक अध्ययन मुख्य रूप से बड़े एकल क्रिस्टल पर केंद्रित रहे हैं। हालाँकि, स्थिर चरण और स्टोइकोमेट्री के साथ इन पदार्थों की पतली फिल्म का प्रायोगिक कार्यान्वयन चुनौतीपूर्ण है। इन पदार्थों की पतली फिल्मों और उनकी हेटरोस्ट्रक्चर स्पिट्रॉनिक्स-आधारित डिवाइस अनुप्रयोगों के लिए वांछनीय हैं। टोपोलॉजिकल और क्वांटम गुणों को कम आयामीता के माध्यम से पतली फिल्मों में और अधिक ट्यून किया जा सकता है। इसके अलावा, पतली फिल्मों अन्य पदार्थों के साथ हेटरोस्ट्रक्चर के निर्माण की अनुमति देती हैं, जो अप्रत्याशित घटनाओं की मेजबानी कर सकती हैं। इसने हमें स्पिट्रॉनिक्स अनुप्रयोगों के लिए  $\text{Fe}_3\text{Sn}_2$  और  $\text{FeSn}$  की पतली फिल्मों और उनके हेटरोस्ट्रक्चर बनाने के लिए प्रेरित किया। इस शोध पुस्तिका में, हम लौहचुंबकीय  $\text{Fe}_3\text{Sn}_2$  और प्रतिलौहचुंबकीय  $\text{FeSn}$  और  $\text{NiO}$  पतली फिल्मों का उत्पादन स्थापित करते हैं। इसके बाद, हम स्पिन पंपिंग व्यवहार का अध्ययन करने के लिए भारी धातु या लौहचुंबकीय ( $\text{FeSn}$  और  $\text{NiO}$  के मामले में) के साथ इन पदार्थों के हेटरोस्ट्रक्चर विकसित करते हैं, जो अगली पीढ़ी के चुंबकीय रिकॉर्डिंग उपकरणों के लिए तकनीकी रूप से महत्वपूर्ण है।

$\text{Fe}_3\text{Sn}_2$  के मामले में, हम सबसे पहले Pt प्रारंभिक परत का उपयोग  $\text{Si}/\text{SiO}_2$  सबस्ट्रेट पर करके पॉलीक्रिस्टलाइन लौहचुंबकीय  $\text{Fe}_3\text{Sn}_2$  पतली फिल्मों के विकास को प्रदर्शित करते हैं। हमारे संरचनात्मक और चुंबकीय माप से संकेत मिलता है कि Pt प्रारंभिक परत के लिए  $M_S = 464 - 640 \text{ emu/cc}$  के उच्च संतृप्ति चुंबकीयकरण के साथ  $\text{Fe}_3\text{Sn}_2$  पतली फिल्मों का एक शुद्ध लौहचुंबकीय चरण बनता है, जबकि Ta प्रारंभिक परत के लिए निम्न  $M_S$  के साथ एक मिश्रित चरण लौहचुंबकीय  $\text{Fe}_3\text{Sn}_2$  और प्रतिलौहचुंबकीय  $\text{FeSn}$  से मिलकर बनता है।  $\text{Fe}_3\text{Sn}_2$  की कागोम संरचना के कारण इलेक्ट्रॉनिक बैंड की भूमिका निर्धारित करने के लिए अनामोलस हॉल प्रभाव माप किए गए थे। हमें एक अशून्य आंतरिक अनामोलस हॉल चालकता ( $\sigma_{\text{int}}$ ), एक बड़ा परिमाण अनामोलस हॉल गुणांक ( $R_s$ ), और अनामोलस हॉल कोण ( $\theta_{\text{AHA}}$ ) मिला जो  $\text{Fe}_3\text{Sn}_2$  पतली फिल्मों में असामान्य हॉल प्रतिरोधकता की आंतरिक उत्पत्ति का संकेत देता है। Pt/ $\text{Fe}_3\text{Sn}_2$  आधारित हेटरोस्ट्रक्चर में किया गया लौहचुंबकीय अनुनाद अध्ययन हमें  $\text{Fe}_3\text{Sn}_2$  की आंतरिक अवमंदन को  $\alpha_{\text{int}} = (3.8 \pm 0.2) \times 10^{-2}$  निर्धारित करने की अनुमति देता है। आगे, Pt/ $\text{Fe}_3\text{Sn}_2$  का स्पिन मिश्रण संचालन  $g_{\text{eff}}^{\uparrow\downarrow} = (11.7 \pm 0.6) \text{ nm}^{-2}$  पाया जाता है, जो अन्य लौहचुंबक/भारी धातु प्रणालियों से तुलनीय है।

FeSn के मामले में, हम  $Al_2O_3$  सबस्ट्रेट पर Pt प्रारंभिक परत का उपयोग करके एपिटैक्सियल फिल्मों के विकास को प्रदर्शित करते हैं। FeSn/  $Ni_{80}Fe_{20}$  बाइलेयर में चुंबकीयकरण माप के साथ-साथ विनिमय पूर्वाग्रह की उपस्थिति का उपयोग करके प्रतिलौहचुंबकीय चरण की पुष्टि की गई थी। FeSn/Py में  $g_{eff}^{\uparrow\downarrow} = (117 \pm 0.6) \text{ nm}^{-2}$  का एक बड़ा स्पिन मिश्रण चालन पाया जाता है जो मानक लौहचुंबक/भारी धातु प्रणालियों की तुलना में परिमाण के लगभग दो-क्रम अधिक है।  $g_{eff}^{\uparrow\downarrow}$  का बड़ा परिमाण उपयोग के लिए और FeSn के कागोम जाली की संभावित भूमिका को इंगित करने के लिए आशाजनक है। हमने प्रतिलौहचुंबकीय NiO/Py सिस्टम में स्पिन पंपिंग की भी जांच की है और हमने दिखाया है कि  $g_{eff}^{\uparrow\downarrow}$  एक अनुकूलित पॉलीक्रिस्टलाइन-NiO/Py प्रणाली उस मूल्य तक पहुंच सकती है जो एक एपिटैक्सियल NiO/Py प्रणाली के लिए है।

शोध पुस्तिका के अंतिम भाग में, हम संख्यात्मक रूप से चुंबकीय क्रांटम सामग्री-आधारित हेटरोस्ट्रक्चर के संभावित अनुप्रयोग का पता लगाते हैं। अगली पीढ़ी के रेसट्रैक मेमोरी उपकरणों के लिए चुंबकीय स्किर्मियन अत्यधिक आशाजनक हैं क्योंकि वे डोमेन-वॉल आधारित रेसट्रैक मेमोरी उपकरणों की तुलना में अल्ट्रा-सघन भंडारण क्षमता और कम बिजली की खपत प्रदान करते हैं। इस शोध पुस्तिका में, हमने रेसट्रैक उपकरणों में लौहचुंबकीय और प्रतिलौहचुंबकीय स्किर्मियन्स की न्यूक्लियेशन प्रक्रिया का संख्यात्मक रूप से अध्ययन किया। हमने प्रतिलौहचुंबकीय सामग्री में इन-प्लेन स्पिन-ध्रुवीकृत धारा का उपयोग करके एक अल्ट्राफास्ट न्यूक्लियेशन सिंगल/मल्टीपल प्रतिलौहचुंबकीय स्किर्मियन पाया। इसके अलावा, हमारी विधि आउट-ऑफ़-प्लेन स्पिन-ध्रुवीकृत धारा की तुलना में इन-प्लेन स्पिन-ध्रुवीकृत धारा का उपयोग करके न्यूक्लियेशन के लिए कम ऊर्जा खपत को भी दर्शाती है। हम Dzyaloshinskii–Moriya इंटरैक्शन का उपयोग किए बिना लौहचुंबकीय  $Fe_3Sn_2$  में बाहरी चुंबकीय क्षेत्रों की एक श्रृंखला के लिए लौहचुंबकीय स्किर्मियन को स्थिर करते हैं।  $Fe_3Sn_2$  में कागोम जाली की मजबूत एकअक्षीय चुंबकीय अनिसोट्रॉपी और द्विध्रुवीय-द्विध्रुवीय अंतःक्रिया स्किर्मियन और एंटी-स्किर्मियन दोनों के न्यूक्लियेशन की सुविधा प्रदान करती है।

# Contents

<b>Certificate</b>	<b>iii</b>
<b>Acknowledgements</b>	<b>v</b>
<b>Abstract</b>	<b>vii</b>
<b>List of Figures</b>	<b>xvii</b>
<b>List of Tables</b>	<b>xxvii</b>
<b>1 Introduction</b>	<b>1</b>
1.1 Quantum Topological Materials and their potential application . . . . .	3
1.2 Motivation of the thesis . . . . .	4
1.3 Organization of Thesis Chapters . . . . .	6
<b>2 Theoretical Background</b>	<b>9</b>
2.1 Introduction . . . . .	9
2.1.1 Magnetism and its type . . . . .	9
2.1.2 Magnetic free energy contributions . . . . .	11
2.2 Magneto-dynamic phenomenon . . . . .	16
2.2.1 Landau-Lifshitz-Gilbert equation . . . . .	16

---

2.2.2	Magnetization damping	17
2.2.3	Ferromagnetic resonance	19
2.3	Hall effects and its mechanism	23
2.3.1	Ordinary Hall effect (OHE)	23
2.3.2	Anomalous Hall effect (AHE)	23
2.3.3	Scaling of conductivity in different regimes	27
2.4	Chiral spin textures	29
2.4.1	Magnetic skyrmion and its types	29
<b>3</b>	<b>Experimental and Numerical Techniques</b>	<b>32</b>
3.1	Deposition techniques	33
3.1.1	Magnetron Sputtering	33
3.1.2	Pulse Laser Deposition (PLD)	34
3.2	Structural Characterization	35
3.2.1	X-ray Diffraction (XRD)	36
3.2.2	X-ray Reflectivity (XRR)	37
3.3	Surface topography characterization	38
3.3.1	Atomic Force Microscopy (AFM)	38
3.3.2	Field Emission Scanning Electron Microscopy (FESEM)	39
3.4	Determination of Composition	40
3.4.1	Energy Dispersive X-Ray (EDX) spectroscopy	40
3.4.2	Electron Probe Microanalysis (EPMA) spectroscopy	41
3.5	Magnetization and transport measurements	42

---

3.5.1	Magnetization measurements . . . . .	42
3.5.2	Transport and Hall measurements . . . . .	44
3.6	Magneto-dynamic measurement . . . . .	45
3.6.1	Ferromagnetic resonance (FMR) measurement . . . . .	45
3.7	Numerical technique . . . . .	48
3.7.1	The micromagnetic approach using Mumax3 software . . . . .	48
<b>4</b>	<b>Growth of kagome ferromagnet <math>\text{Fe}_3\text{Sn}_2</math> films and spin pumping in Pt/<math>\text{Fe}_3\text{Sn}_2</math></b>	<b>50</b>
4.1	Introduction . . . . .	51
4.2	Experimental Details . . . . .	53
4.2.1	Growth optimization of thick $\text{Fe}_3\text{Sn}_2$ films . . . . .	53
4.2.2	Growth optimization of ultra-thin $\text{Fe}_3\text{Sn}_2$ films . . . . .	54
4.3	Results and Discussion . . . . .	55
4.3.1	Structural, magneto-static, and magneto-transport properties of 70 nm-thick $\text{Fe}_3\text{Sn}_2$ films . . . . .	55
4.3.2	Structural, magneto-static, magneto-transport, and magnetodynamic properties of ultra-thin $\text{Fe}_3\text{Sn}_2$ films . . . . .	64
4.4	Summary . . . . .	70
<b>5</b>	<b>Growth of kagome antiferromagnet <math>\text{FeSn}</math> films and spin pumping in <math>\text{FeSn}/\text{Py}</math></b>	<b>71</b>
5.1	Introduction . . . . .	72
5.2	Experimental Details . . . . .	73
5.2.1	Growth optimization of metallic $\text{FeSn}/\text{Py}$ bilayer . . . . .	73
5.3	Results and discussion . . . . .	75
5.3.1	Structural properties of epitaxial- $\text{FeSn}$ and $\text{FeSn}/\text{Py}$ system . . . . .	75

5.3.2	Magnetic measurements and study of spin pumping in FeSn/Py . . . . .	76
5.4	Summary . . . . .	80
<b>6</b>	<b>Growth of antiferromagnetic NiO films and spin pumping in NiO/Py</b>	<b>82</b>
6.1	Introduction . . . . .	82
6.2	Experimental Details . . . . .	84
6.2.1	Growth optimization of NiO/Py bilayer . . . . .	84
6.3	Results . . . . .	85
6.3.1	Study of structural properties in epitaxial-and polycrystalline-NiO/Py . . . . .	85
6.4	Discussion . . . . .	88
6.4.1	Study of spin pumping in epitaxial-NiO/Py . . . . .	88
6.4.2	Study of spin pumping in polycrystalline-NiO/Py . . . . .	90
6.5	Summary . . . . .	92
<b>7</b>	<b>Numerical study of the nucleation of magnetic skyrmions</b>	<b>94</b>
7.1	Introduction . . . . .	95
7.2	Numerical Details . . . . .	96
7.2.1	Material parameters: AFM skyrmion . . . . .	98
7.2.2	Material parameters: FM skyrmion . . . . .	98
7.3	Results and Discussion . . . . .	99
7.3.1	Nucleation study of single/multiple AFM skyrmions with DMi . . . . .	99
7.3.2	Nucleation study of single/multiple FM skyrmions without DMi . . . . .	109
7.4	Summary . . . . .	116

<b>8 Summary and Future Outlook</b>	<b>117</b>
8.1 Summary of Thesis . . . . .	117
8.2 Major outcomes . . . . .	118
8.3 Future Outlook . . . . .	120
<b>Bibliography</b>	<b>121</b>
<b>Publication</b>	<b>141</b>
<b>Conference</b>	<b>142</b>
<b>Biodata</b>	<b>145</b>

# List of Figures

1.1	Schematic representation of (a) Dirac nodes present in Dirac semimetals, and (b) Weyl nodes with opposite chiralities present in Weyl semimetals due to breaking of either inversion symmetry or time-reversal symmetry. The sign of chirality $\chi = +1(-1)$ indicates monopoles (anti-monopoles) of Weyl nodes. . . . .	3
2.1	A schematic of magnetic spin texture that has been achieved due to competition between exchange energy and DM energy: (a) A ferromagnet with a positive $J_{ex}$ and zero $D$ , (b) A ferromagnet with a positive $J_{ex}$ and non-zero $D$ , (c) an anti-ferromagnet with a negative $J_{ex}$ and zero $D$ ,(d) an anti-ferromagnet with a negative $J_{ex}$ and non-zero $D$ . . . . .	13
2.2	Schematic of precession magnetization as a function of (a) only effective magnetic field ( $H_{\text{eff}}$ ), and (b) combined effect of the effective magnetic field ( $H_{\text{eff}}$ ) and damping terms as per Eq. (2.19). (c) $H_{\text{eff}}$ with the microwave rf-field to excite and balance the dissipative torque originated due to the Gilbert damping. . . . .	17
2.3	Schematic of spin relaxation of magnetization due to (a) intrinsic damping of FM and (b) effective damping of FM including the additional damping caused by spin pumping into the NM. . . . .	20
2.4	Schematic diagram for transport measurement in the ordinary Hall effect and anomalous Hall effect geometry. . . . .	24
2.5	Schematic diagram of deflection of electrons in Hall geometry originated due to (a) intrinsic scattering, (b) skew scattering, and (c) side-jump scattering mechanism. The concept of this schematic is adapted from Ref. [1] . . . . .	26

2.6	Scaling of transverse conductivity ( $\sigma_{xy}$ ) with the longitudinal resistivity ( $\sigma_{xx}$ ), taken from ref. [2]. . . . .	28
2.7	Schematic of the skyrmion configurations: (a) top view and (b) side view. $\alpha$ and $\phi$ are the space angle in the plane and the in-plane magnetization angle, respectively with respect to the x-axis. . . . .	29
2.8	Illustrations of magnetic skyrmions in different chirality: (a) Néel-type skyrmion (b) Bloch-type skyrmion, (a) Anti-skyrmion, and (d) Antiferromagnetic skyrmion. . . . .	30
3.1	Schematic diagram of thin film growth process using magnetron sputtering technique. . . . .	34
3.2	Schematic showing the main chamber of the pulse laser deposition system. . . . .	35
3.3	(a) Measurement geometries for X-ray diffraction technique. (b) Schematic of X-Ray diffraction from the crystal planes in a sample. . . . .	36
3.4	Schematic of XRR measurements, (a) the incident X-ray with the incident angle ( $\theta_1 < \theta_C$ ) and (b) the incident X-ray with the incident angle ( $\theta_2 > \theta_C$ ). (c) The symbols represent measured XRR patterns for a film. The black lines correspond to the fit to the data. . . . .	37
3.5	Schematic of atomic force microscopy technique. . . . .	39
3.6	Schematic representation of the vibrating sample magnetometer from Quantum Designs. . . . .	43
3.7	Schematic diagram of the current-carrying and voltage-sensing contacts in (a) linear and (b) Hall contact geometry. . . . .	45
3.8	Schematic diagram of FMR setup, which consists of electromagnet magnets powered by DC power supply, Helmholtz coil, CPW, rf signal generator, microwave diode, gaussmeter with Hall probe and the computer. . . . .	46

- 4.1 (a) The structure of  $\text{Fe}_3\text{Sn}$  kagome plane in  $\text{Fe}_m\text{Sn}_n$ -system. The  $\text{Fe}_3\text{Sn}$  kagome lattice consists of corner-sharing Fe triangles arranged in a hexagonal manner, and the centre of the hexagons is occupied by Sn atoms. The unit cell of (b) ferromagnetic:  $\text{Fe}_3\text{Sn}_2$  and (c) antiferromagnetic:  $\text{FeSn}$  shows the different stacking of  $\text{Fe}_3\text{Sn}$  and  $\text{Sn}_2$  layers. . . . . 51
- 4.2 (a) X-ray reflectivity data for the  $\text{Fe}_3\text{Sn}_2$  (upper panel),  $\text{Ta}/\text{Fe}_3\text{Sn}_2$  (middle panel) and  $\text{Pt}/\text{Fe}_3\text{Sn}_2$  (bottom panel) thin films. The solid cyan lines represent the fit to the data using Parratt's formalism. (b) GIXRD pattern for the  $\text{Fe}_3\text{Sn}_2$  thin films deposited without and with Ta and Pt seed layers. All the films are grown at room temperature and annealed at 500 °C for 1 hour. The peaks due to the antiferromagnetic  $\text{FeSn}$  phase are shown as green dashed lines, while the peaks due to the ferromagnetic  $\text{Fe}_3\text{Sn}_2$  phase are shown as red dashed lines. The plus symbol, open circle symbol, and closed circle symbol represent the experimental data for  $\text{Fe}_3\text{Sn}_2$ ,  $\text{Ta}/\text{Fe}_3\text{Sn}_2$  and  $\text{Pt}/\text{Fe}_3\text{Sn}_2$  thin films, respectively. . . . . 56
- 4.3 Atomic force microscopy images of (a)  $\text{Ta}/\text{Fe}_3\text{Sn}_2$  and, (b)  $\text{Pt}/\text{Fe}_3\text{Sn}_2$ . (c) MFM images for pure ferromagnetic  $\text{Pt}/\text{Fe}_3\text{Sn}_2$  for a scan area of ( $5 \times 5 \mu\text{m}^2$ ) measured at room temperature. (d) spectrum line profile of topography (top) and MFM phase shift (bottom) corresponding to the MFM image of  $\text{Pt}/\text{Fe}_3\text{Sn}_2$  thin film. . . . . 57
- 4.4 (a) MFM images for pure ferromagnetic  $\text{Pt}/\text{Fe}_3\text{Sn}_2$  for a scan area of ( $5 \times 5 \mu\text{m}^2$ ) measured at room temperature. (b) spectrum line profile of topography (top) and MFM phase shift (bottom) corresponding to the MFM image of  $\text{Pt}/\text{Fe}_3\text{Sn}_2$  thin film. . . . . 58
- 4.5 Temperature-dependent magnetization curves for (a)  $\text{Pt}/\text{Fe}_3\text{Sn}_2$  and, (b)  $\text{Ta}/\text{Fe}_3\text{Sn}_2$ . (c) The behavior of coercive field  $H_C$  and (d) Saturation magnetization  $M_S$  as a function of temperature for both the samples. . . . . 59
- 4.6 Micro-magnetically simulated magnetization curve for 100% FM domains ( $\text{Pt}/\text{Fe}_3\text{Sn}_2$ ) and 50% FM domains ( $\text{Ta}/\text{Fe}_3\text{Sn}_2$ ). On the left-hand side, Symbol 'a', 'b', 'c', and, 'd' show the saturation field ( $\approx \pm 3$  T) for both cases. On the right-hand side, shows the snapshots of the respective y component of magnetization ( $M_y/M_S$ ) for both the cases at ( $\approx \pm 0.3$  T). . . . . 60

- 4.7 Magnetic field dependence of the transverse Hall resistivities (a) for Pt and (b) Ta seed layered  $\text{Fe}_3\text{Sn}_2$  thin films at various temperatures (inset shows the schematic of Hall geometry setup with current flowing along the  $x$ -axis and magnetic field normal to the  $xy$  plane). The red lines represent the linear fit of Hall resistivity  $\rho_{xy}$  (for  $B > 1$  T region). (c, d) Anomalous Hall resistivity  $\rho_{xy}^{AHE}$  and longitudinal resistivity  $\rho_{xx}$  as a function of temperature for the Pt and Ta seed layered  $\text{Fe}_3\text{Sn}_2$  thin films. (e) Anomalous Hall conductivity  $\sigma_{xy}^{AHE}$  as a function of the square of longitudinal conductivity  $\sigma_{xx}^2$  and the black solid line is fit to the data. (f) Scaling coefficient  $S_H$  as a function of temperature for the Pt and Ta seed layered  $\text{Fe}_3\text{Sn}_2$  thin films. The filled red circles and open green circles represent the experimental data for Pt/ $\text{Fe}_3\text{Sn}_2$  and Ta/ $\text{Fe}_3\text{Sn}_2$ , respectively. . . . . 61
- 4.8 (a) Schematic of Ta/Pt/ $\text{Fe}_3\text{Sn}_2$ / $\text{AlO}_x$  thin film stack. (b) X-ray diffraction (XRD) spectrum obtained for the various thicknesses ( $t$ ) of  $\text{Fe}_3\text{Sn}_2$ . (c) 2D-view of AFM image of ( $5 \mu\text{m} \times 5 \mu\text{m}$ ) scan area of 2 nm thin  $\text{Fe}_3\text{Sn}_2$  film. (d) The solid symbols represent the respectively measured X-ray reflectivity (XRR) plot for all thicknesses of  $\text{Fe}_3\text{Sn}_2$  thin film and the solid line represents the fit to the corresponding XRR plot. (e) The open symbols indicate the variation in interfacial roughness data obtained from the XRR technique and the closed symbols indicate the variation in surface roughness data obtained from the AFM technique. . . . . 64
- 4.9 Magnetic hysteresis loop obtained at room temperature for 5 nm ultra-thin  $\text{Fe}_3\text{Sn}_2$  film when the external field is swept parallel to the film surface. . . . . 65
- 4.10 The transverse Hall resistivity ( $\rho_{xy}$ ) obtained at room temperature for a 5 nm ultra-thin  $\text{Fe}_3\text{Sn}_2$  film when the external field is swept perpendicular to the film surface. The open and closed symbol represents the  $\rho_{xt}$  for only  $\text{Fe}_3\text{Sn}_2$  and Ta/Pt/ $\text{Fe}_3\text{Sn}_2$ / $\text{AlO}_x$  film stack. The black dashed arrow indicates the anomalous Hall resistivity ( $\rho_{xx}^{\text{Fe}_3\text{Sn}_2}$ ) for only  $\text{Fe}_3\text{Sn}_2$ . . . . . 66
- 4.11 Frequency dependence of measure FMR spectrum for  $\text{Fe}_3\text{Sn}_2$ (5 nm) thin film. The open gradient symbol and black solid line represent the experimental data and corresponding fit using Eq. (3.2). . . . . 68

- 4.12 (a) Frequency ( $f$ ) plotted as function of resonance field ( $H_R$ ) and corresponding fit with Kittel Eq. 3.4. (b) The plot of the extracted value of  $M_{\text{eff}}$  with the thickness of ferromagnet ( $t_{\text{FM}}$ ), inset shows the variation of  $M_{\text{eff}}$  with the inverse of  $t_{\text{FM}}^{-1}$  and corresponding fit with Eq. 3.5. (c) The variation of linewidth ( $\Delta H$ ) with frequency ( $f$ ) and corresponding fit with linewidth Eq. 3.6. (d) Effective damping constant ( $\alpha_{\text{eff}}$ ) as a function of  $t_{\text{FM}}$ , inset shows the plot of  $\alpha_{\text{eff}}$  inverse of inverse thickness  $t_{\text{FM}}^{-1}$  and corresponding fit with Eq. 2.25. The solid open symbols and lines represented the experimental data and the fit, respectively. . . . . 69
- 5.1 (a) Schematic of the FeSn crystal structure, which contains the kagome lattice arrangement of Fe atoms (blue symbol) with Sn atoms (yellow symbol) at the center of the hexagon. The red arrow indicates the orientation of the magnetic moment of Fe atoms. (b) and (c) Schematics of the Kagome lattice (top view), along with the illustration of destructive quantum interference induced due to electron confinement, (d) corresponding band diagram showing the Dirac cone and flat band. Figures (c) and (d) are adapted from Ref [3] . . . . . 72
- 5.2 Structural characterization using (a)  $\theta-2\theta$  XRD scan measured for Pt(5 nm)/FeSn(30 nm). (b) The color gradient plot represents the fine range  $\theta - 2\theta$  scan for Pt(5 nm)/FeSn(30 nm)/Py( $t$  nm) thin films. (c) This plot represents the  $\phi$ -scan measurements for Pt(5 nm)/FeSn(30 nm) film. (d) This plot represents the rocking curve ( $\omega$ -scan) for the Pt(5 nm)/FeSn(30 nm). The triangular symbol and black line represent the measured data and fitted line to the  $\omega$ -scan scan, respectively. . . . . 75
- 5.3 (a) The hysteresis plot with a dominating diamagnetic contribution of substrate measured at room temperature ( $T = 300$  K) for FeSn(30 nm) film and only substrate. (b) The closed square and circle symbols represent the normalized hysteresis plot measured at room temperature ( $T = 300$  K) for FeSn(30 nm)/Py(5 nm) and FeSn(30 nm)/Py(15 nm), respectively. (c) The open square and circle symbols represent the corresponding hysteresis plot of FeSn(30 nm)/Py(5 nm) and FeSn(30 nm)/Py(15 nm) bilayers measured at 2 K, after field cooling in 6 T from 300 K. . . . . 77

- 5.4 FMR spectrum over the frequency range 3-9 GHz for (a) FeSn(30 nm)/Py(15 nm) and (a) Ref: Py(15 nm) thin film. The solid black lines represent the fitted line with the Lorentzian Eq. 3.2. . . . . 78
- 5.5 (a)-(e) The dependence of  $f$  versus  $H_R$  and (f)-(j)  $\Delta H$  versus  $f$  for the FeSn(30 nm)/Py( $t$  nm) and Ref: Py( $t$  nm) films. The symbols represent experimental data, while the black lines represent fits. . . . . 79
- 5.6 The variation of (a)  $M_{\text{eff}}$  and (b)  $\alpha_{\text{eff}}$  with the inverse thickness ( $t_{\text{Py}}^{-1}$ ) of Py layer. (c) The value of effective spin mixing conductance ( $g_{\text{eff}}^{\uparrow\downarrow}$ ) of FeSn/Py thin film and comparing it with our own Ref: Py sample as well as reported values. The closed and open diamond symbols represent the experimental data of FeSn(30 nm)/Py( $t$  nm) and Ref: Py( $t$  nm) films, respectively, while the black lines represent the fit to the experimental data. . . . . 80
- 6.1 (a) Schematic of the nickel oxide (NiO) crystal structure, where yellow and blue symbols signify the nickel (Ni) and oxygen (O) atoms, respectively. (b) Schematic of sample stacking for polycrystalline and epitaxial NiO-based multilayers. . . . . 83
- 6.2 (a) XRD pattern Poly.(NiO)/Py/Pt thin film on Si/SiO<sub>2</sub> substrate measured in glancing incidence geometry. (b) XRD pattern in Gonio-mode ( $\theta - 2\theta$ ) for Epi. (NiO)/Py/Pt thin film deposited on Al<sub>2</sub>O<sub>3</sub>(0001) substrate, and inset represents corresponding  $\phi$ -scan. (c) Green symbols represent the rocking curve ( $\omega$ -scan) for NiO (111) reflection in Epi.(NiO)/Py/Pt thin film. (d) XRR plots for Poly.(NiO)/Py/Pt and Epi.(NiO)/Py/Pt thin films. The solid black line represents the fits to extract the thickness, density, and roughness of the film stack. 86
- 6.3 (a) Schematic of a co-planar waveguide-based FMR setup.  $H$  and  $h_{rf}$  are the external magnetic and RF excitation fields, respectively. (b) FMR ( $\theta_H = 90^\circ$ ) spectra for Poly.(NiO)/Py/Pt and Epi.(NiO)/Py/Pt thin film in the In-plane configuration. (c) FMR ( $\theta_H = 0^\circ$ ) spectra for Poly.(NiO)/Py/Pt and Epi.(NiO)/Py/Pt thin film in the out-of-plane configuration. The symbols are experimental data, while the lines represent fits. . . . . 87

- 6.4  $f$  versus  $H_R$  in (a) out-of-plane FMR ( $\theta_H = 0^\circ$ ) and (b) In-plane FMR ( $\theta_H = 90^\circ$ ) configuration for Epi.(NiO)/Py/Pt thin film. The inset in (b) represents the in-plane  $M$  versus  $H$  for Epi.(NiO)/Py/Pt thin film. (c)  $f$  versus  $H_R$  data for Ref: Py/Pt.  $\Delta H$  versus  $f$  in (d) out-of-plane FMR ( $\theta_H = 0^\circ$ ) and (e) in-plane FMR ( $\theta_H = 90^\circ$ ) configuration for Epi.(NiO)/Py/Pt thin film. (f)  $f$  versus  $H_R$  data for Ref: Py/Pt. The symbols and lines were used to represent the experimental data and the fit, respectively. . . . . 89
- 6.5 (a) In-plane FMR ( $\theta_H = 90^\circ$ ) spectra for Poly.(NiO)/Py/Pt thin film and, (c) out-of-plane FMR ( $\theta_H = 0^\circ$ ) spectra for Poly.(NiO)/Py/Pt thin film. Whereas symbol and line were used to represent the experimental data and fitted line, respectively. . . . . 92
- 7.1 (a) Snapshots during nucleation of AFM skyrmion at the different instants of time when a current pulse with a width  $\tau = 5.5$  ps is applied. Here, (green/red) circle represents current pulses (ON/OFF). The current is injected in a circular region with diameter,  $d_n = 70$  nm. The diameter of the AFM skyrmion is found to be  $d_s = 32$  nm after 20 ps. (b) The evolution of topological charge  $Q_A$  for sublattice  $A$  (open symbols) and  $Q_B$  of sublattice  $B$  (closed symbols) during the nucleation of the AFM skyrmion. . . . . 99
- 7.2 Change in total energy density  $\Delta W$  during the nucleation of AFM skyrmion for varying pulse widths ( $\tau_w = 4.5, 5.0, 5.5,$  and  $6.0$  ps). (b) the corresponding evolution of topological charge  $Q_A$  for sublattice  $A$  (open symbols) and  $Q_B$  of sublattice  $B$  (closed symbols). . . . . 100
- 7.3 Dependence of inverse of threshold pulse width (black circles) and nucleation time (red squares) on the current density for (a) in-plane, and (b) out-of-plane spin-polarized cases. The trajectory of single AFM moments at fixed current density ( $J_{x,z} = J_{z,z} = 6.5 \times 10^{13}$  A/m<sup>2</sup>) for (c) in-plane and (d) out-of-plane cases. The color in (c) and (d) represents the time elapsed and  $t = 0$  ps represents the time instant when the pulse is injected. . . . . 102

- 7.4 Left figures (a-c) show the evolution of topological charge for the AFM skyrmion sub-lattices  $A$  (open symbols) and sub-lattice  $B$  (closed symbols) for three different pulse widths ( $t_w = 0.7, 3.1$  and  $12.8$  ps) for a constant current density ( $J_{x,z} = 3 \times 10^{13}$  A/m<sup>2</sup>). Right figures (d-f) show the corresponding snapshots of AFM skyrmions at 200 ps for each case. . . . . 105
- 7.5 (a) Time evolution of topological charge at ( $T = 300$  K) for sub-lattice  $A$  (open symbols) and  $B$  (closed symbols). (b) Variation of threshold pulse width on the temperature at fixed current density ( $J_{x,z} = 1 \times 10^{13}$  A/m<sup>2</sup>). . . . . 108
- 7.6 (a)  $M_Z$  and  $Q_S$  as function of  $H_{\text{ext}}$  are represented by blue and green solid line. The letter a, b, c, d, e, and f represents the schematics of FM square lattice of film at different  $H_{\text{ext}}$ . . . . . 110
- 7.7 The variation of topological charge  $Q_S$  (upper panel) and skyrmion radius  $r_S$  (lower panel) as a function of the external magnetic field  $H_{\text{ext}}$ . Inset images represent the corresponding snapshot of FM skyrmion in Fe<sub>3</sub>Sn<sub>2</sub> taken at different  $H_{\text{ext}}$ . . . . . 111
- 7.8 (a) The schematic of Bloch and anti-skyrmion states in Fe<sub>3</sub>Sn<sub>2</sub> nanotrack geometry with a dimension of ( $2 \mu\text{m} \times 0.5 \mu\text{m} \times 8$  nm). Zoomed view of (b) Bloch-type skyrmion and (c) anti-skyrmion configurations in Fe<sub>3</sub>Sn<sub>2</sub> with the value of  $W$ ,  $P$ , and  $Q_S$ . . . . . 112
- 7.9 (a) The evolution of topological charge value in different regions  $R_1$ ,  $R_2$ ,  $R_3$ ,  $R_4$ , and  $R_F$  of the Fe<sub>3</sub>Sn<sub>2</sub> nanotrack represented by an open circle, square, triangle, star and diamond symbol, respectively. (b) The real space topography of skyrmion/anti-skyrmion nucleation on increasing the external magnetic field perpendicular to the plane of Fe<sub>3</sub>Sn<sub>2</sub> nanotrack. Here,  $H_1$ ,  $H_2$ ,  $H_3$ , and  $H_4$  indicate the respective  $H_{\text{ext}}$  for the nanotrack. . . . . 113

7.10 (a) The variation of  $E_{\text{therm.}}$  and  $E_{\text{Total}}$  over the temperature range from 0 K to 300 K at fixed  $H_4 = 24$  mT. (b) The variation of  $Q_S$  was numerically calculated using Eq. (7.3) for all the regions ( $R_1$ - $R_4$ ) of the  $\text{Fe}_3\text{Sn}_2$  nanotrack. (c) The snapshot image taken for the fixed  $H_4 = 24$  mT and  $T=300$  K of the  $\text{Fe}_3\text{Sn}_2$  nanotrack with an isolated anti-skyrmion. The thermal energy ( $E_{\text{therm.}}$ ) is denoted by green open squares and the total energy ( $E_{\text{Total}}$ ) is denoted by a red open circle). . . . . 115

# List of Tables

4.1	The magnetic and structural properties of $\text{Fe}_3\text{Sn}_2$ and $\text{FeSn}$ . The data shown are taken from Refs. [4–6] . . . . .	52
4.2	Element and composition analysis for $\text{Pt}/\text{Fe}_3\text{Sn}_2$ and $\text{Ta}/\text{Fe}_3\text{Sn}_2$ thin film. . . . .	54
4.3	Comparison of magneto-transport properties of $\text{Fe}_3\text{Sn}_2$ thin films grown on Ta and Pt seed layer at 300 K. . . . .	62
5.1	Extracted values of exchange bias field ( $H_{\text{ex.}}$ ), in-plane saturation field ( $H_{\text{S}}$ ), and saturation magnetization ( $M_{\text{S}}$ ) at temperature 300 K and 2 K. . . . .	77
5.2	Summary of experimentally measured effective spin mixing conductance ( $g_{\text{eff}}^{\uparrow\downarrow}$ ) in our $\text{FeSn}/\text{Py}$ heterostructures and various other magnetic heterostructures reported in the literature. . . . .	80
7.1	Summary of Figure 4: Dependence of total nucleation time on current pulse width for multiple AFM skyrmions. . . . .	106